RSC Advances

PAPER

View Article Online
View Journal | View Issue

Cite this: *RSC Adv.*, 2025, **15**, 1665

Unveiling the structural aspects of novel azo-dyes with promising anti-virulence activity against MRSA: a deep dive into the spectroscopy *via* integrated experimental and computational approaches†

Ahmed M. Hegazy, *[ab] Michael G. Shehat,[c] Alaa. Abouelfetouh,[cd] Mohamed Teleb,[efg] Sherine N. Khattab*[a] and Nesreen S. Haiba[h]

A novel series of azo dyes was successfully synthesized by combining amino benzoic acid and amino phenol on the same molecular framework *via* azo linkage. The structural elucidation of these dyes was carried out using various spectroscopic techniques, including UV-vis, FT-IR, NMR spectroscopy, and HRMS. Surprisingly, the aromatic proton in some dyes exhibited exchangeability in D_2O, prompting a 2D NMR analysis to confirm this phenomenon. Furthermore, comprehensive density functional theory (DFT) calculations were conducted to unravel synthetic dyes' geometrical and electronic properties. Meanwhile, the reactivity of various sites was further investigated through Frontier Molecular Orbitals (FMOs) analysis and molecular electrostatic potential mapping. Besides, the experimental NMR spectra were interpreted by incorporating theoretically computed NMR spectrum and reduced density gradient (RDG) function. These computations revealed a pronounced intramolecular hydrogen bond through O–H···N interaction that significantly influenced the proton chemical shift. The dyes were assessed for their antimicrobial activities using agar diffusion, micro broth dilution, and biofilm inhibition assays. Interestingly, one of the synthetic dyes showed promising antibacterial effects against *S. aureus* (ATCC-6538) as well as against a multidrug-resistant MRSA clinical isolate with a MIC (minimum inhibitory concentration) of 78.12 μg mL^{-1}. Moreover, that dye inhibited biofilm formation of the strong biofilm former clinical MRSA isolate with a concentration as low as 0.25 MIC (19.53 μg mL^{-1}). Indeed, our qPCR data suggest that inhibiting the SaeS/SaeR system is another potential mechanism by which **D4** exerts its antibacterial and anti-virulence effects. Altogether, this shows these synthetic azo dyes' promising antibacterial and anti-virulence activities concerning MRSA clinical infections.

Received 3rd September 2024
Accepted 13th December 2024

DOI: 10.1039/d4ra06367h

rsc.li/rsc-advances

1 Introduction

The spread of antibiotic resistance has engendered profound public health concerns, leading to the WHO declaration of AMR as one of the top 10 global health threats, requiring immediate attention.[1,2] Among the numerous multi-resistant microorganisms, methicillin-resistant *Staphylococcus aureus* (MRSA) has stood out as an exceptionally dangerous bacterium in recent decades, resulting in nosocomial infections, and community-acquired bacterial infections that can be life-threatening.[3] This pathogenic ability of MRSA is mainly related to its resistance to antibiotics belonging to different classes and its carriage of multiple virulence determinants, allowing it to evade the immune defenses and counteract antimicrobial chemotherapy.[4] Numerous researchers are orienting their research efforts toward improving innovative treatments for infectious diseases to address this point. Within this realm, azo dyes have garnered considerable attention as a class of chemical compounds with

[a]*Chemistry Department, Faculty of Science, Alexandria University, Alexandria 21321, Egypt. E-mail: sherinekhattab@alexu.edu.eg; ahmed.hegazy@alexu.edu.eg*
[b]*Department of Materials Science, Institute of Graduate Studies and Research, Alexandria University, Alexandria, Egypt*
[c]*Department of Microbiology and Immunology, Faculty of Pharmacy, Alexandria University, 21521 Alexandria, Egypt*
[d]*Department of Microbiology and Immunology, Faculty of Pharmacy, Alamein International University, 51718 Alamein, Egypt*
[e]*Department of Pharmaceutical Chemistry, Faculty of Pharmacy, Alexandria University, 21521 Alexandria, Egypt*
[f]*Cancer Nanotechnology Research Laboratory (CNRL), Faculty of Pharmacy, Alexandria University, 21521 Alexandria, Egypt*
[g]*Department of Medicinal Chemistry, Faculty of Pharmacy, Alamein International University (AIU), Alamein City 5060310, Egypt*
[h]*Department of Physics and Chemistry, Faculty of Education, Alexandria University, Egypt*

† Electronic supplementary information (ESI) available. See DOI: https://doi.org/10.1039/d4ra06367h

potential therapeutic applications against various diseases. Azo dyes are a well-established class of organic compounds encompassing the linkage of primary aromatic amine and activated coupler through chromophoric –N=N– bonds.[5,6]

An azo group's linkage of aromatic moieties causes an extended conjunction primarily responsible for dyes' color chemistry.[7] Unexpectedly, azo dyes were discovered accidently when William Henry Perkin synthesized a purple dye known as mauveine in 1856.[8–11] Subsequently, azo dyes were included in various applications, including chemical sensors,[12] indicators,[11] and printing inks.[13] In addition to the primary application of azo dyes as a colorant, azo dyes were reported as potential bacteriostatic,[14] fungicidal,[15] anti-cancer agents,[16] and carriers for drug delivery.[17] Indeed, some dyes were utilized as innovative therapeutic agents.[18] For instance, methylene blue has been utilized in treating methemoglobinemia and as a potential neuroprotective agent in Alzheimer's disease research.[19]

A further example is indocyanine green, a fluorescent dye employed in medical imaging to assess liver function and cardiac output.[20] Another unique aspect is that some specific azo dyes have demonstrated excellence in photodynamic therapy by generating reactive oxygen species following light activation, destroying the cancer cells.[21] Among all pharmacological applications, azo dyes exhibited outstanding antibacterial activity.[6,22] Mechanistically, Gerhard Domagk concluded that the antimicrobial activity of prontosil (an amino sulphonamide azo dye) is mainly attributed to the toxic product generated after the reduction of the azo group.[23] This reduction process can be accomplished by azoreductases in human and animal intestinal microbiota, yielding the corresponding aromatic amine.[24] Alternatively, azo dyes can bind to several metal ions, forming complexes demonstrating antibacterial properties by inhibiting DNA replication through several pathways.[25] Therefore, it is evident that the research focus revolves around the design and synthesis of novel azo dyes that possess exceptional antibacterial properties. More specifically, dyes that include a coupler with amino groups are anticipated to exhibit more activity than other dyes. Despite the publication of various research papers aimed at advancing the field of antibacterial activity of dyes, there are remaining gaps that need to be tackled in this area. Nevertheless, the synthesis of azo dyes can be a challenging process. The difficulty could be attributed to the potential occurrence of self-coupling,[26] the generation of several products,[27] and the specific requirements for preserving the diazonium salt stable during the entire reaction period.[28,29] Furthermore, the spectroscopic characteristics of dyes are occasionally mysterious. This could be attributed to geometrical isomerization across the –N=N– bond and the great possibility of tautomerization.[30–33]

At this stage, it is crucial to incorporate quantum chemical calculations for structural elucidation and theoretical spectra computations. With the development of quantum computing technologies, there is an excellent advancement in computational chemistry.[34] Where accurate methods could lead to a substantial interpretation of chemical problems. Although several methods are used to predict the geometry of molecules and spectroscopic properties, density functional theory (DFT) remains superior to most other methods.[35–38] Researchers often choose to use DFT as a calculation method due to the compensation between the precision of theoretical results and the processing time required.[39–41]

In this study, we designed a series of novel azo dyes derived from isomeric amino benzoic acid coupled with isomeric amino phenols in an acidic medium. All synthetic dyes were characterized by different spectroscopic techniques such as UV-vis, FT-IR, NMR spectroscopy and high-resolution mass spectra (HRMS). Additionally, comprehensive DFT calculations were conducted to reveal synthetic dyes' geometrical and electronic properties besides spectroscopic data interpretation. The experimental NMR spectra have been extensively interpreted by combining the computed NMR spectrum and the reduced density gradient (RDG) function to unravel the noncovalent interaction (NCI) contributing to the unique chemical shifts. Impressively, an aromatic proton in certain dyes was exchangeable in D_2O. For these reasons, a 2D NMR experiment was conducted to verify the exchangeability of this aromatic proton.

Further relevant molecular characteristics, including Frontier Molecular Orbitals (FMOs) and molecular electrostatic potential maps (MEP), were also computed to elaborate structural reactivity. The dyes were assessed for their antimicrobial and anti-virulence activities against different *Staphylococcus aureus* strains. Considering the structural aspects of synthetic dyes, it can be regarded as a potent antibacterial agent.

2 Experimental and computational methods

All chemicals utilized in this research have been obtained from Alfa Aesar and used without additional processes. TLC analysis was conducted on Merck silica gel plates with aluminium backing. The appropriate solvent systems were used, and the spots were detected using a Spectroline UV lamp at either 254 or 365 nm.

2.1. Measurements and instruments

The electronic (UV-vis) spectra were recorded in ethanol as a solvent on a Shimadzu double-beam UV-visible spectrophotometer (Model No. UV 1800). Fourier transform infrared spectra (FT-IR) were collected using Bruker Tensor 37 FT-IR spectrometer with KBr pellets in the 500–4000 cm^{-1} range. The NMR spectra for the synthetic dyes were obtained using a 500 MHz JEOL NMR spectrometer with deuterated DMSO-d_6 as solvent. The chemical shift values δ are presented in parts per million (ppm), and the spectra were calibrated using residual solvent as an internal reference. Meanwhile, the coupling constant J values were reported in Hz. An LC/Q-TOF, 6350 (Agilent Technologies, Santa Clara, CA, USA) instrument was utilized to acquire the high-resolution mass spectral data using the electrospray ionization method. The melting points were determined through MEL-Temp II equipment with open capillaries without further correction.

2.2. The general methodology for the synthesis of dyes D1–D4

The dyes were synthesized by adjusting the molar ratio to match the reaction's stoichiometry.[42] The synthesis started by

introducing (2.00 g, 14.50 mmol) of isomeric amino benzoic acid in 10 mL of 0.729 M sodium carbonate solution; the solution was stirred until complete solubilization. The solution was cooled, and sodium nitrite (1.01 g, 14.50 mmol) was added. The diazotization process was initiated by the dropwise addition of 2 M HCl. Afterwards, the mixture was stirred in an ice bath for 2–3 hours and checked by TLC for the completion of diazotization. To start the coupling reaction, (1.58 g, 14.50 mmol) of isomeric amino phenol as an activated coupler was dissolved in 7.24 mL of 2 M HCl and added carefully to the diazonium salt solution over 1 hour. The solution was further stirred for 1–2 hours till the completion of the coupling reaction monitored by TLC. The solution was neutralized with sodium carbonate until the desired dyes were precipitated entirely. The precipitated dyes were filtered and washed several times with cold and hot water and dried under a vacuum to afford the pure desired product. A schematic diagram of the synthesis process is shown in Fig. 1.

2.2.1. 2-((4-Amino-2-hydroxyphenyl)diazenyl)benzoic acid (D1). Dye **D1** was obtained as red powder, 2.75 g (73.22%) yield; melting: 251–253 °C; FT-IR (KBr); 3666–2914 (br, OH), 3508 (phenolic OH), 3321, 3138 (NH_2), 1680 (C=O carboxylic acid), 1490 (N=N), cm^{-1}; ^{1}H-NMR (500 MHz: DMSO-d_6): δ isomer I (80%): 5.44 (brs, 2H, NH_2, D_2O exchangeable), 6.15–6.22 (m, 1H, Ar–H), 6.60 (d, J = 10 Hz, 1H, 1Ar–H), 7.20–7.30 (m, 1H, 1Ar–H), 7.35–7.70 (m, 2H, 2Ar–H), 7.71 (d, J = 9.5 Hz, 1H, 1Ar–H), 7.81–7.87 (m, 1H, Ar–H), 8.94 (brs, 1H, COOH, D_2O exchangeable), 14.43 (s, 1H, OH, D_2O exchangeable). Isomer II (20%): 5.44 (brs, 2H, NH_2, D_2O exchangeable), 6.15–6.22 (m, 1H, Ar–H), 6.39 (d, J = 10 Hz, 1H, 1Ar–H), 7.20–7.30 (m, 1H, 1Ar–H), 7.35–7.70 (m, 2H, 2Ar–H), 7.78 (d, J = 9.5 Hz, 1H, 1Ar–H), 7.81–7.87 (m, 1H, Ar–H), 8.94 (brs, 1H, COOH, D_2O exchangeable), 14.43 (s, 1H, OH, D_2O exchangeable). ^{13}C-NMR (125 MHz: DMSO-d_6): δ 163.76, 161.39, 140.56, 138.27, 136.27, 136.92, 131.24, 130.85, 129.90, 127.81, 126.67, 116.32, 115.76, 98.73. Elemental analysis calculated for molecular formula $C_{13}H_{11}N_3O_3$: C, 60.70; H, 4.31; N, 16.33. Found: C, 60.97; H, 4.67; N, 16.05.

2.2.2 3-((4-Amino-2-hydroxyphenyl)diazenyl)benzoic acid (D2). Dye **D2** was obtained as orange powder, 3.07 g (81.86%) yield; melting: 233–235 °C; FT-IR (KBr): 3504–2991 (br, OH), 3415 (phenolic OH), 3340, 3207 (NH_2), 1683 (C=O carboxylic acid), 1479 (N=N) cm^{-1}; ^{1}H-NMR (500 MHz: DMSO-d_6): δ isomer I (87.13%): 5.95 (s, 1H, Ar–H), 6.31 (dd, J_1 = 9 Hz, J_2 = 1.8 Hz, 1H, Ar–H), 6.73 (brs, 2H, NH_2, D_2O exchangeable), 7.40 (d, J = 10 Hz, 1H, 1Ar–H), 7.53–7.57 (m, 1H, 1Ar–H), 7.86 (t, J = 8.6 Hz, 2H, 2Ar–H), 8.16 (s, 1H, 1Ar–H), 13.01 (brs, 1H, COOH, D_2O exchangeable), 14.10 (s, 1H, OH, D_2O exchangeable). Isomer II (12.87%): 6.15 (dd, 1H, Ar–H), 6.19 (s, 1H, Ar–H), 6.73 (brs, 2H, NH_2, D_2O exchangeable), 7.53–7.57 (m, 2H, 2Ar–H), 7.70 (d, J = 10 Hz, 1H, 1Ar–H), 7.92–7.98 (m, 2H, Ar–H), 8.24 (s, 1H, 1Ar–H), 13.01 (brs, 1H, COOH, D_2O exchangeable), 14.10 (s, 1H, OH, D_2O exchangeable). ^{13}C-NMR (125 MHz: DMSO-d_6): δ 167.64, 160.68, 156.57, 149.94, 134.22, 132.61, 131.45, 130.26, 128.85, 125.12, 120.37, 99.14. Elemental analysis calculated for molecular formula $C_{13}H_{11}N_3O_3$: C, 60.70; H, 4.31; N, 16.33. Found: C, 60.93; H, 4.66; N, 16.01.

2.2.3. 4-((4-Amino-2-hydroxyphenyl)diazenyl)benzoic acid (D3). Dye **D3** was obtained as red powder, 3.34 g (89.06%) yield; melting: 225–227 °C; FT-IR (KBr): 3670–2817 (br, OH), 3533 (phenolic OH), 3369, 3172 (NH_2), 1680 (C=O carboxylic acid), 1465 (N=N), cm^{-1}, ^{1}H-NMR (500 MHz: DMSO-d_6): δ isomer I (80%): 5.96 (s, 1H, Ar–H), 6.41 (d, J = 11 Hz, 1H, 1Ar–H), 7.45 (brs, 2H, NH_2, D_2O exchangeable), 7.69 (d, J = 10 Hz, 2H, 2Ar–H), 7.94–8.09 (m, 3H, 3Ar–H), 10.77 (s, 1H, COOH, D_2O

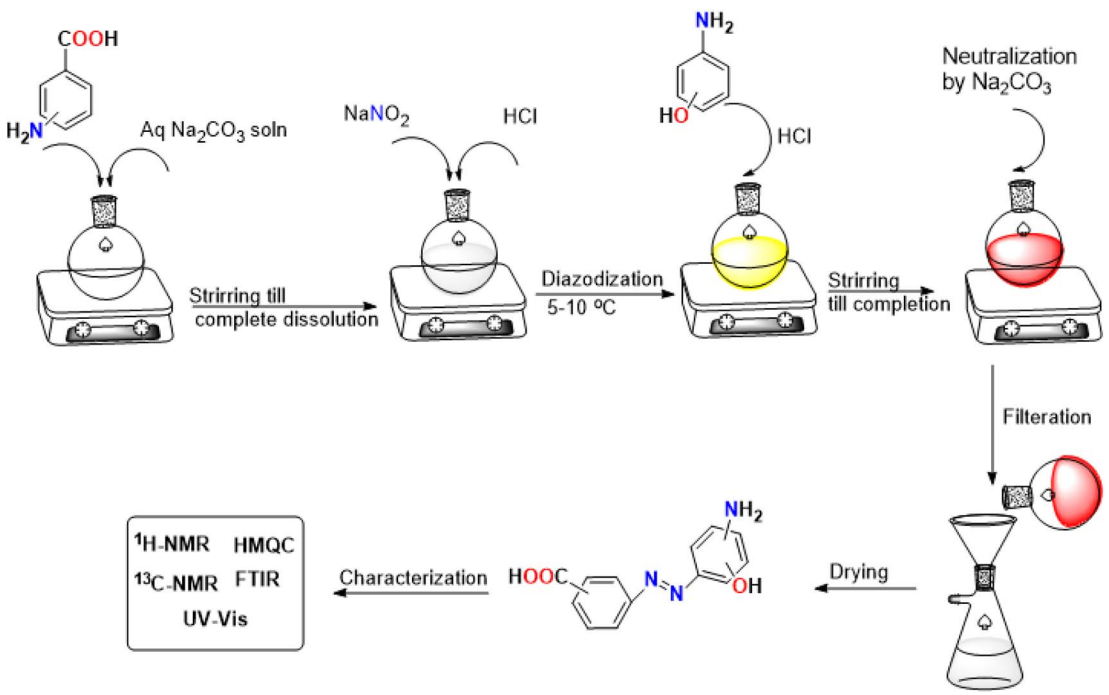

Fig. 1 A schematic diagram depicting the step-by-step process for synthesizing dyes D1–D4.

exchangeable), 14.39 (s, 1H, OH, D_2O exchangeable). Isomer II (20%): 6.20–6.24 (m, 1H, Ar–H), 6.59–6.70 (m, 1H, 1Ar–H), 7.45 (brs, 2H, NH_2, D_2O exchangeable), 7.56–7.63 (m, 2H, 2Ar–H), 7.83 (d, $J = 10$ Hz, 1H, 1Ar–H), 7.94–8.09 (m, 2H, 2Ar–H), 10.77 (s, 1H, COOH, D_2O exchangeable), 14.39 (s, 1H, OH, D_2O exchangeable). ^{13}C-NMR (125 MHz: DMSO-d_6): δ 167.53, 164.48, 132.03, 130.99, 128.83, 121.49, 118.92, 101.05, 99.02. Elemental analysis calculated for molecular formula $C_{13}H_{11}N_3O_3$: C, 60.70; H, 4.31; N, 16.33. Found: C, 60.88; H, 4.65; N, 16.12.

2.2.4. 3-((4-Amino-3-hydroxyphenyl)diazenyl)benzoic acid (D4). Dye **D4** was obtained as red powder, 1.105 g (29.46%) yield; melting: 160 °C dec; FT-IR (KBr): 3710–2741 (br, OH), 3498 (phenolic OH), 3300, 3200 (NH_2), 1711 (C=O carboxylic acid), 1460 (N=N) cm^{-1}; ^{1}H-NMR (500 MHz: DMSO-d_6): δ isomer I (60%): 6.72–6.76 (m, 1H, Ar–H), 7.03–7.09 (m, 1H, 1Ar–H), 7.15 (brs, 1H, Ar–H), 7.31–7.34 (m, 1H, Ar–H), 7.48–7.51 (m, 1H, Ar–H), 7.64–7.66 (m, 1H, Ar–H), 7.89–7.97 (m, 3H, 1Ar–H + NH_2, D_2O exchangeable), 8.21 (brs, 1H, Ar–H), 9.72 (s, 1H, COOH, D_2O exchangeable), 12.54 (brs, 1H, OH, D_2O exchangeable). Isomer II (40%): 6.68–6.70 (m, 1H, Ar–H), 7.03–7.09 (m, 2H, 2Ar–H), 7.28–7.29 (m, 1H, Ar–H), 7.58–7.61 (m, 1H, Ar–H), 7.70–7.71 (m, 1H, Ar–H), 7.89–7.97 (m, 2H, NH_2, D_2O exchangeable), 8.21 (brs, 1H, Ar–H), 9.72 (s, 1H, COOH, D_2O exchangeable), 12.54 (brs, 1H, OH, D_2O exchangeable). ^{13}C-NMR (125 MHz: DMSO-d_6): δ 168.45, 167.60, 153.05, 149.34, 144.76, 129.44, 121.93, 118.55, 114.99, 112.73, 104.06. Elemental analysis calculated for molecular formula $C_{13}H_{11}N_3O_3$: C, 60.70; H, 4.31; N, 16.33. Found: C, 60.88; H, 4.65; N, 16.12.

2.3. Computational methods

All quantum chemical calculations performed during this study were done through Gaussian 09 software along with Gauss View 5.0.[43] The DFT method was selected for all computations, employing the Becke 3–Lee–Yang–Parr (B3LYP) functional in conjunction with standard 6-311++G(d,p) basis sets.[44,45] All calculations started by optimizing the geometry of the synthetic dyes; subsequently, vibrational frequency calculations were performed to confirm that the optimized geometries were global minima at the potential energy surface. Further optimization in DMSO solvent was performed using the Conductor-like Polarizable Continuum model (CPCM) to model the solvent effect.[46] Besides, the nuclear shielding constant was computed based on the GIAO method, from which the theoretical chemical shifts were computed.[47] We used Vesta software, Gauss View 5.0, and ChemCraft 1.8 to visualize frontier molecular orbitals, MEP, and optimized geometries, respectively.[48–50] Different NCI within the molecule were elucidated through the RDG function through Multiwfn and Visual Molecular Dynamics (VMD) software.[51,52]

2.4. Assessment of the antimicrobial activity of the different dyes

2.4.1. Microorganisms. This study was approved by the Alexandria University Ethical Committee (0306796). The strains used in this study were *Staphylococcus aureus* (reference strain ATCC-6538) in addition to one multi-drug-resistant methicillin-resistant *Staphylococcus aureus* (MRSA) clinical isolate (obtained from the isolates repertoire at the Department of Microbiology and Immunology at Faculty of Pharmacy, Alexandria University) (this isolate is a hospital-acquired clinical strain isolated from the pus of inpatient admitted at Alexandria Main University Hospital). The isolate was determined to be resistant to ciprofloxacin, cefoxitin, levofloxacin, chloramphenicol, tetracycline, gentamicin, rifampicin as well as fusidic acid, which was done by disc diffusion assays.

2.4.2. Determination of the minimum inhibitory concentration (MIC) and minimum bactericidal concentration (MBC). The broth microdilution method was used to determine the MIC of each tested dye using Mueller–Hinton broth (MHB) as outlined in CLSI guidelines.[53] Briefly, colonies were taken directly from fresh agar plates and were suspended in 0.9% NaCl. The turbidity of the microorganism suspension was adjusted to that of the 0.5 McFarland standard. The suspension was further diluted 100 fold in 2× cation-adjusted MHB to reach the final bacterial concentration of 10^6 CFU mL^{-1}.[54] Next, two fold serial dilutions of the dyes in sterile water were prepared to obtain the desired concentration range. Then, 100 μL of the bacterial suspension in 2× MHB was added to each well of a sterile 96 well plate containing 100 μL of the tested sample or solvent control. The positive control wells contained bacterial suspension without the tested sample. The plates were then incubated for 24 h at 37 °C. The MIC was defined as the lowest concentration that completely inhibited the growth of the bacteria. The same procedure was done for MIC determination against *S. aureus* ATCC 6538 as well as the MRSA clinical isolate. For MBC determination, the clear wells that showed no growth in the MIC experiment were further diluted in MHB. After the new plates were incubated for 24 h at 37 °C, the results were interpreted for each tested dye whether to be bacteriostatic (if all the wells showed regrowth of the organism) or bactericidal (if the concentration corresponding to the MIC showed no regrowth following dilution in the MBC experiment). The MBC was then determined for bactericidal dyes as the lowest concentration that ultimately killed the tested bacteria.[55]

2.4.3. Bacterial growth curves. To investigate the effect of **D4** on the growth curves of MRSA clinical isolate, we incubated the isolate with different sub-inhibitory concentrations of **D4**; then, we conducted bacterial count at various time points. The starting bacterial inoculum was 5×10^5 CFU mL^{-1} (same inoculum size used for MIC determination);[54] the tubes were then incubated without or with different concentrations of **D4** equivalent to 0.5, 0.25 and 0.125× MIC values. The tubes were incubated at 37 °C in an orbital shaking incubator (190 rpm), and samples were taken from each tube at 3, 6 and 24 hour time points, serially diluted, and then plated onto Muller–Hinton agar. The bacterial count was calculated for each condition and time point using the corresponding dilution factor, and the bacterial growth curves were plotted using GraphPad Prism software.

2.4.4. Biofilm inhibition assay. As previously described, the biofilm formation assay was conducted in a 96 well microtiter plate using the crystal violet assay[56] with slight modifications. **D4** dye was used in this assay as it was the most potent one, as determined by the MIC assay. Bacterial suspensions of the MRSA isolate were cultured in Brain Heart Infusion (BHI)

supplemented with 1% glucose and were adjusted to obtain a bacterial concentration of 10^6 CFU mL^{-1}. The bacterial suspension was inoculated in each well either alone (control) or in combination with the different concentrations of **D4.** The plate was incubated for 24 h at 37 °C under static conditions, after which the wells were decanted and washed with 1× PBS three times, then fixed with 2% formaldehyde for one minute. The adherent biofilm was stained with 200 μL 0.5% crystal violet for 30 min at room temperature. Excess stain was removed by washing thrice with 200 μL 1× PBS, then left to dry in an inverted position at Room Temperature (RT) overnight. The bound crystal violet was solubilized using 95% ethanol in a shaking incubator for one hour and quantified by measuring absorbance at OD_{595} nm using an ELISA reader (BioTek, USA). The percent biofilm mass was calculated for each **D4** concentration relative to the control untreated bacterial-formed biofilm (OD of wells treated for each concentration/OD of control untreated wells × 100).

2.4.5. Quantitative real-time polymerase chain reaction (qRT-PCR). The expression levels of the genes saeR and saeS, playing a role in staphylococcal virulence, were detected in the clinical MRSA isolate in the presence or absence of **D4** using qRT-PCR. The bacterial subcultures were grown either with **D4** at its 0.5× MIC concentration or with DMSO solvent control for 24 hours. The cells were centrifuged at 6000 rpm for 10 min, and the supernatant layer was discarded. The pellets were then washed once and subjected to total RNA extraction using spin columns according to the manufacturer's instructions (Applied Biotechnology, Egypt). The quality of the extracted RNA was assessed using the Nanodrop microvolume spectrophotometer (Thermo Fisher, USA). Complementary DNA (cDNA) was synthesized from extracted RNA by reverse transcription using hexamer random primers according to the manufacturer's instructions (Applied Biotechnology, Egypt). qPCR was done using specific primers for the SaeR and SaeS two-component system (Table 1)[57,58] using SYBR Green master mix in a BioRad CFX96 real-time PCR system (BioRad, United States). Relative gene expression was analyzed using $\Delta\Delta C_t$ values compared to the housekeeping gyrB gene. Data were presented as mean ± SEM of the different replicates. Statistical analysis was done using a Student's *t*-test to compare the expression level of each gene at 0.5× MIC of **D4** compared to negative solvent-treated control.

Table 1 Primers used in this study

Primer	Sequence
SaeR_F	GTCGTAACCATTAACTTCTG
SaeR_R	ATCGTGGATGATGAACAA
SaeS_F	TGTATTTAAAGTGATAATATGAGTC
SaeS_R	CTTAGCCCATGATTTAAAAACACC
Gyr_F	CCAGGTAAATTAGCCGATTGC
Gyr_R	AAATCGCCTGCGTTCTAGAG

3 Results and discussion

3.1. Synthesis and structural perspectives

Dyes **D1–D4** were synthesized through diazotization of amino benzoic acid isomers, followed by coupling with isomeric amino phenols (Scheme 1). Since diazonium salts may undergo coupling reactions in both acidic and basic conditions, we conducted the coupling process in an acidic medium. Indeed, the selection of an acidic medium in our work is attributed to the fact that coupling with amino phenols in the basic medium can lead to numerous coupling products, which decrease the yield and purity of the targeted product.

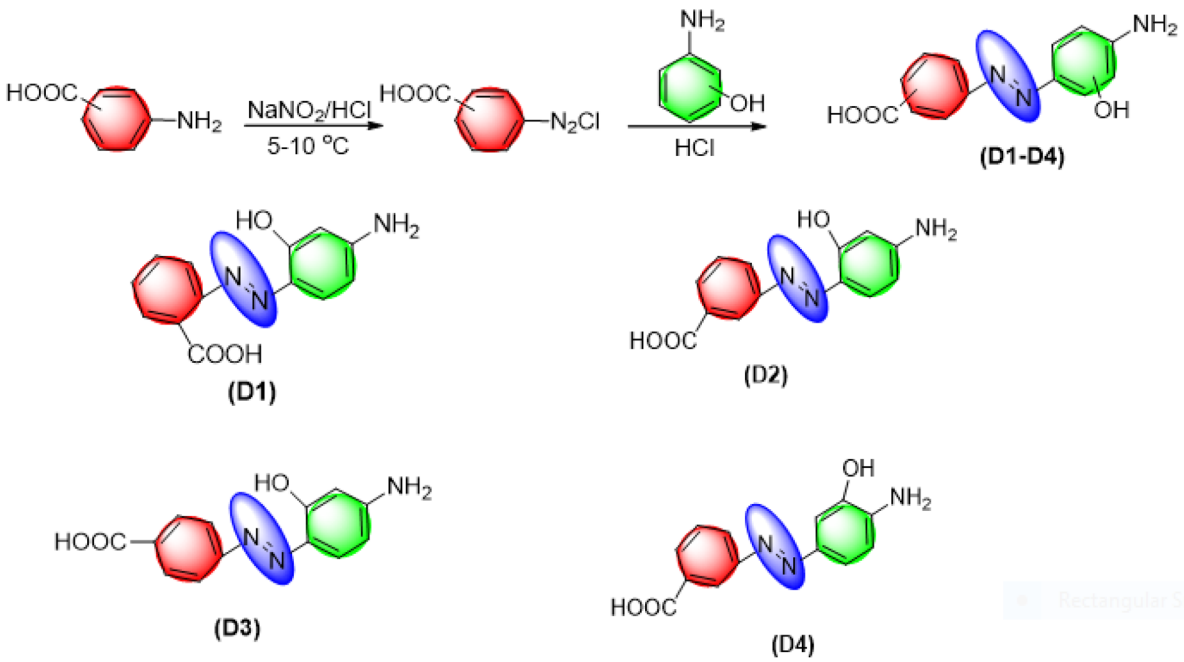

Scheme 1 The synthetic pathway for the dyes D1–D4 and their corresponding structures.

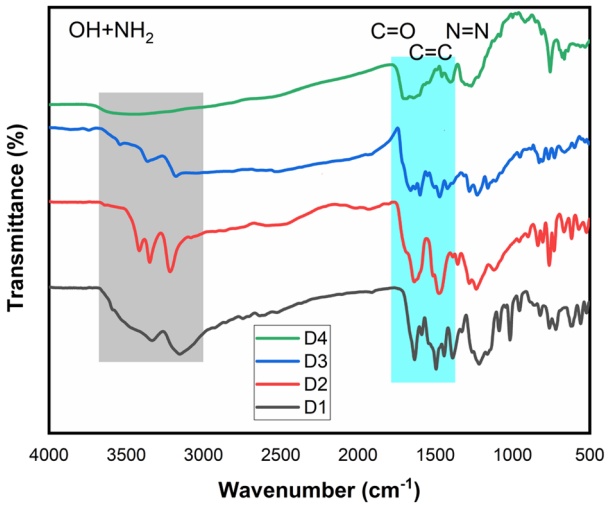

Fig. 2 The stacked FT-IR spectra for synthetic dyes D1–D4.

After the completion of the reactions, dyes **D1–D4** were subjected to various spectroscopic techniques, including UV-vis, FT-IR, (^{1}H and ^{13}C) NMR spectroscopy, and HRMS to confirm their structures. Further characterization by Heteronuclear Multiple Quantum Coherence (HMQC) was selectively performed for dye **D2** as a representative structure for dyes to unravel 1-bond coupling. Another structural aspect of dyes is their geometrical structure. Since dyes can exist in either the syn form or the anti-one, the designation of the geometrical structure of dyes is a must. A key factor for the designation of geometrical forms is the thermodynamic stability of various geometrical isomers. It is reported that most dyes are thermodynamically more stable when they exist in the anti-form.[59] This might be caused by the decreased electrostatic repulsive forces between the coupler structure and the amine.[60] For these reasons, all computational calculations were performed for the anti-form of the dyes. Alternatively, some dyes in our work exist in both geometrical forms, confirmed by a relative comparison of the integration in ^{1}H-NMR spectroscopy.

3.2. Vibrational spectroscopy analysis

Vibrational spectroscopy is crucial in characterizing organic molecules, particularly in identifying their functional groups. Fig. 2 presents the stacked FT-IR spectra of synthetic dyes **D1–D4**, revealing several critical observations. Initially, all dyes exhibit a broad band in the 2741–3710 cm^{-1} range and a sharp peak around 3000 cm^{-1}. These overlapping bands correspond to hydroxyl groups and the characteristic aromatic C–H vibrational band. Although amino groups typically display two distinct stretching vibrational bands centered at approximately 3100 and 3300 cm^{-1}, these modes are not always detectable in the synthetic dyes under study. This is likely due to the broadness of the hydroxyl group bands, which obscure the amino group vibrational modes.

Furthermore, all dyes show three other fundamental vibrational modes around 1680–1711, 1600, and 1460–1490 cm^{-1}, consistent with the expected structural features of these synthetic dyes. A detailed analysis reveals that the 1680–1711 cm^{-1} peak is associated with the carbonyl group of carboxylic acid functionalities. The peak around 1600 cm^{-1} is likely due to the stretching vibration of C=C within the aromatic rings of the amine or the coupler. Finally, the peak near 1460 cm^{-1} indicates the presence of an azo group, confirming the linkage between the amine and the coupler structure.[61]

3.3. UV-vis analysis

UV-visible spectroscopy is an invaluable technique for elucidating electronic transitions within organic dyes, providing critical insights into their photophysical properties. The UV-vis spectra for synthesized dyes **D1–D4** are shown in Fig. 3. Accordingly, various insightful conclusions can be formulated. Concerning dyes **D1–D3** derived from *m*-amino phenol, they exhibit two characteristic bands centered at 270 nm and 430–440 nm. The constancy of spectral band positions for these dyes implies that shifting of carboxylic acid substituent has a minor impact on the light absorption properties of dyes **D1–D3**. A careful examination of the origin of these two bands leads to assigning the electronic transitions responsible for these spectral bands. The band located around 270 nm is predominantly attributed to π–π* transition, while the band situated in the 430–440 nm region is associated with n–π* transition.

In comparison, dye **D4** derived from *o*-amino phenol demonstrated two unique bands at 210 and 350 nm originating from π–π* and n–π* transitions, respectively. A particularly meaningful research question explores how altering the position of the hydroxyl group within the coupler structure influences the electronic spectra, specifically of **D2** and **D4**. Notably, there is a significant hypsochromic shift for dye **D4**. This positioning of the hydroxyl group relative to the amino group mainly causes this decrease. One potential explanation of this phenomenon is that the existence of the hydroxyl group in the *ortho* position relative to the amino group hinders the capability of an amino group to contribute to the conjugation; hence, λ_{max} decreases. This observation aligns perfectly with the *ortho* effect

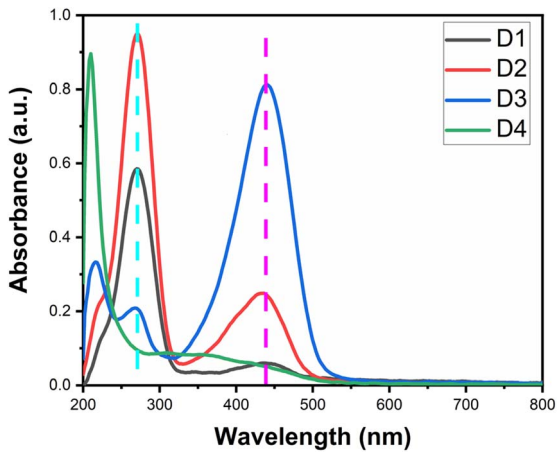

Fig. 3 UV-vis spectra for the synthetic dyes D1–D4 in ethanol.

observed frequently in aromatic compounds where the *ortho* substituent causes a considerable decline in λ_{max} when compared to other positions.[31,62]

3.4. NMR interpretation

NMR spectroscopy is the most effective spectroscopic technique for identifying the chemical structure of synthesized organic compounds. The NMR spectra of dyes **D1–D4** are shown in the ESI.† While NMR spectra of dye **D2** are shown in Fig. 4 as operational spectra for illustration. The interpretation begins by focusing on the most deshielded protons, typically those of the carboxyl group within the amine structure and the hydroxyl group within the coupler structure. The hydroxyl group within the coupler structure for dyes **D1–D3** was observed at 14.10–14.43 ppm. The intramolecular hydrogen bonding between the proton of the hydroxyl group and the nitrogen of the azo functional group mainly drives this substantial downfield effect.

To further confirm this hypothesis, we computed the theoretical chemical shifts for dye **D2** based on the same basis set and method pertained in all calculations but in DMSO solvent. The computed spectrum is shown in Fig. 4d. Remarkably, the hydroxyl proton was the most deshielded proton, with a computed chemical shift of 14.12 ppm. Along with this, the computed bond length for O–H···N was found to be 1.683 Å, a typical value for stable intramolecular hydrogen bonds. These results were in excellent agreement with the experimental findings.

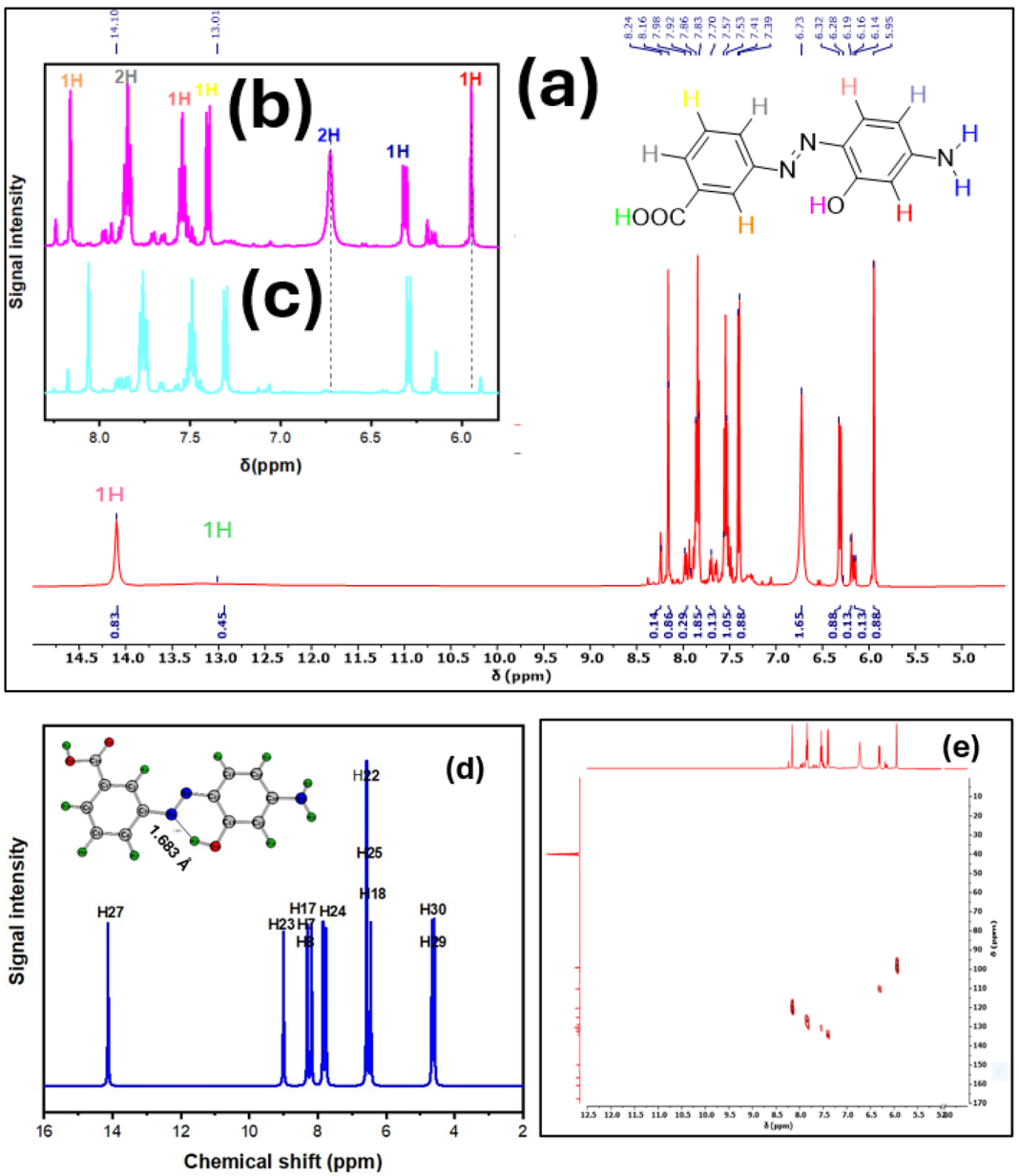

Fig. 4 (a) Experimental ^{1}H-NMR spectrum of dye **D2**. (b) The expanded aromatic region from ^{1}H-NMR spectrum of dye **D2**. (c) The expanded aromatic region from the ^{1}H-NMR spectrum of dye **D2** in the presence of D_2O. (d) Computed ^{1}H-NMR spectrum of dye **D2** in DMSO. (e) HMQC spectrum of dye **D2**.

Moreover, we performed the NMR analysis with the inclusion of deuterium oxide (D_2O), and the resulting spectrum is shown in Fig. 4c. Significantly, the peak has disappeared, indicating that this proton is exchangeable and attached to the heteroatom. These results match those observed in earlier studies for *o*-hydroxy azo compounds.[63–66]

Compared to dye **D4**, the hydroxyl group proton was observed at 9.72 ppm. This significant difference in the chemical shift is ascribed to the positioning of the hydroxyl group. In the case of dye **D4**, the hydroxyl group is far away from the azo group, and there is no chance of intramolecular hydrogen bond formation with the azo group. Another highly deshielded proton is the carboxylic group proton, which appeared for most of the dyes as a broad peak around 8.94–13.01 ppm and wholly disappeared in the presence of D_2O. The amino group protons were observed in the 5.44–7.97 ppm range for dyes **D1–D4**. Also, these peaks vanished in D_2O.

Unique results were obtained regarding the analysis of aromatic protons region. First of all, the relative comparison of $Z:E$ isomers percent was calculated from the integration values. The aromatic protons were observed within the 5.95–8.21 ppm chemical shift range. We will interpret the spectra of **D2** as a representative example. The most shielded aromatic proton was the one adjacent to the amino and hydroxyl groups, which appeared as a singlet peak at 5.95 ppm. This might be explained by the strong electron-donating capability of these groups, which leads to an increase in electron density in the surrounding region and a decline in the chemical shift.

On the contrary, the most deshielded aromatic proton was the one situated *ortho* to the azo and carboxylic acid groups. This proton experiences a singlet peak at 8.10–8.20 ppm. This increase in chemical shift is allocated to the electron-withdrawing effect of the neighbouring functional groups, which renders the adjacent proton in deshielded regions; thus, the chemical shift increases. Concurrently, a triplet peak is observed at 7.80–7.90 ppm, probably attributed to the two protons *ortho* to the carboxylic acid group and the azo group separately. The last three protons were observed at 7.50–7.60, 7.40, and 6.30 ppm. The proton observed at 7.50–7.60 is assigned to be the one *ortho* to the azo group within the coupler structure. On the other hand, the proton observed at 6.30 ppm is expected to be the one *ortho* to the amino group only. Finally, the remaining proton is the *meta* to the azo and carboxylic groups.

A highly debated research question emerges from the experimental spectra depicted in Fig. 4a–c. It is evident that in the presence of D_2O, the peak intensity at 5.95 ppm significantly decreases. This observation warrants further investigation since this peak corresponds to an aromatic proton. To interpret this unexpected phenomenon, we must employ additional spectroscopic techniques to elucidate the one-bond C–H correlation. Using these spectroscopic data, we can determine whether this exchangeable proton is bonded to carbon or not.

One of the well-established methods for examining proton-carbon coupling and correlations is 2D-NMR spectroscopy, specifically Heteronuclear Multiple Quantum Coherence (HMQC). For our study, we performed an HMQC spectrum for compound **D2**, as shown in Fig. 4e. Notably, we observed a correlation between the peak at 5.95 ppm in the ^{1}H-NMR and the peak at 98.96 ppm in the ^{13}C-NMR.

These findings confirm that the aromatic proton in question is exchangeable in D_2O. The exchangeability of aromatic protons has been previously discussed in the literature, marking a significant advancement in kinetics and reaction mechanism investigations.[69–71]

3.5. HRMS analysis

The high-resolution mass spectrum stands as a cornerstone technique for precisely determining the molecular weights of organic compounds. The mass spectral data for dyes **D1–D4** were presented in the ESI.† Despite their similar molecular weights, the fragmentation patterns of these dyes tell a tale of divergence. For dyes **D2–D4**, the expected dominant peak emerges at $[M + 1]^{+\bullet} = 258.087$ (Fig. S8, S12, and S16 (ESI)†), a predictable outcome that aligns with theoretical predictions. However, then comes dye **D1** (Fig. S4†), which has a mass spectrum that requires further understanding. Instead of following the anticipated path, for dye **D1** exhibits its most intense peak at a substantially higher *m/z* value. One plausible explanation is the formation of adducts, where a stable intermediate interacts with other species, giving rise to unexpected products.[67]

This hypothesis supports the unique structural features of dye **D1**. Here, the carboxyl and hydroxy groups are positioned *ortho* to the azo group, setting the stage for fascinating chemical dynamics. Literature suggests that *ortho*-substituted benzoic acid derivatives, under specific conditions, can undergo cleavage to form a ketene intermediate.[68] This reactive species could further interact with the dye, culminating in the observed increase of the molecular ion peak.

3.6. FMOs analysis

Despite the continuous advancements in computing molecular reactivity descriptors, the Frontiers Molecular Orbitals (FMOs) stand out as one of the most crucial reactivity descriptors.[72] FMOs primarily identify two distinct orbitals: the highest occupied molecular orbital (HOMO), which is strongly localized to moieties within the molecule that acts as electron donors. Nevertheless, the lowest unoccupied molecular orbital (LUMO) is vital in deciding the regions within the molecule that can act as an electron acceptor. The energy gap between HOMO and LUMO is a distinctive reactivity descriptor that gives pivotal information about a molecule's stability and biological activity.[73]

Fig. 5 provides essential information about the moieties within the synthetic dyes responsible for charge donation and acceptance. The charge distribution density in HOMO is predominantly a π character localized over the aromatic rings, azo group, and a considerable contribution from heteroatoms at the coupler ring. Meanwhile, the carboxyl group has a minor contribution to HOMO, which completely disappears in dyes **D2** and **D4**. A closer inspection of the energy values of HOMO for the newly synthesized dyes leads to the conclusion that **D2** has

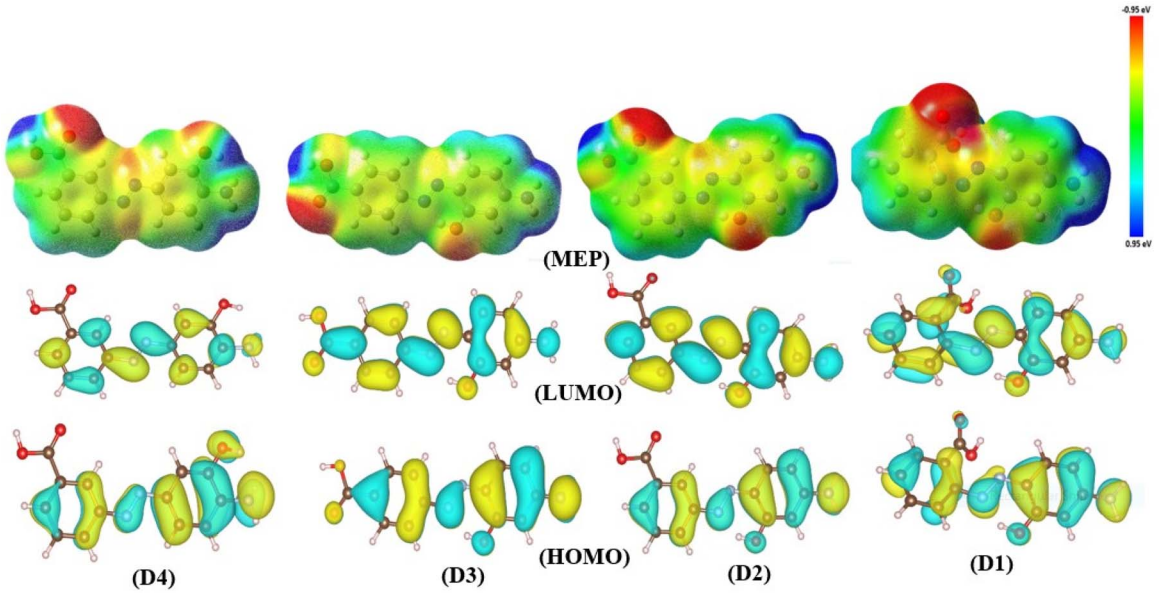

Fig. 5 Graphical representation of HOMO, LUMO, and MEP maps for the synthesized **D1–D4** dyes.

the most pronounced potential as a donor structure. This is evident from its HOMO energy, which is typically −5.915 eV. However, the dye with the minor capability for charge donation is **D3**, with a typical value for $E_{HOMO} = -6.168$ eV.

Another significant aspect of reactivity is examining the charge distribution density within the LUMO. A comprehensive interpretation of charge distribution density from Fig. 5 shows that the LUMO is somehow distributed over the entire molecule, primarily exhibiting a π* character. The energy values analysis also demonstrated that the dye with the highest electrophilic character is **D3**, with a typical energy for LUMO equal to −2.900 eV. Conversely, dye **D4** experienced the lowest reactivity towards being a charge acceptor with a typical value for energy of the LUMO = −2.538 eV.

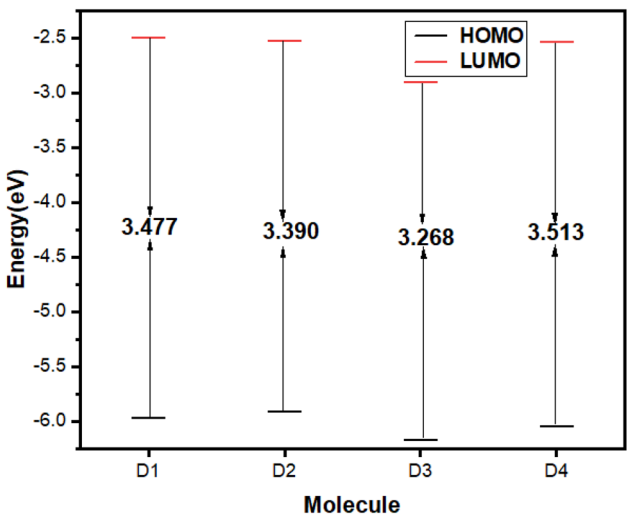

Fig. 6 HOMO–LUMO energy gap for the synthesized azo-dyes **D1–D4**.

Having discussed the FMOs analysis, it is crucial to analyze the energy gap data, which provides a comprehensive basis for comparing the reactivity of different dyes. The energy gap plots for dyes are shown in Fig. 6. Among these dyes, the dye with the highest susceptibility towards the excitation of charges from HOMO to LUMO is **D3**, with a typical energy gap value of 3.268 eV. Nonetheless, dye **D4** exhibits remarkable stability with a typical energy gap of 3.513 eV.

3.7. MEP analysis

The molecular electrostatic potential is a distinctive function that reveals the molecular regions prone to electrophilic and nucleophilic attacks. MEP values are visualized through color-coded plots that indicate these reactive areas. The MEP color codes encompass a spectrum, where red denotes regions with the most considerable negative potential, identifying nucleophilic sites. In contrast, blue areas exhibit the highest electrophilicity, and green regions are neutral. It's important to note that reduced color intensity signifies weaker interactions. These plots are vital for understanding biological reactivity and molecular recognition.[74]

Fig. 5 displays the MEP maps for the newly synthesized dyes. These results show that the red regions correspond to areas near the most electronegative atom, typically oxygen. The intense red color shifts across the iso-density surface, particularly near the hydroxyl and carboxylate groups on the aromatic rings. Additionally, regions around the azo group, the nitrogen of the amino group, and the aromatic ring cores are highlighted in yellow. This yellow color results from stabilizing the test-positive charge by the electrostatic attraction with nearby electrons. A much-interesting question is the existence of yellow color within the aromatic moieties, which could be ascribed to the existence of π electronic density. Due to their electrophilic nature, the hydrogen atoms attached to the aromatic ring and

Table 2 Computed quantum chemical descriptors for synthetic dyes D1–D4

Molecular descriptor	(D1)	(D2)	(D3)	(D4)
E_{HOMO} (eV)	−5.972	−5.915	−6.168	−6.051
E_{LUMO} (eV)	−2.495	−2.525	−2.900	−2.538
η (eV)	1.738	1.695	1.634	1.756
σ $(eV)^{-1}$	0.575	0.589	0.611	0.569
χ (eV)	4.233	4.220	4.534	4.294
μ (eV)	−4.233	−4.220	−4.534	−4.294
μ_o (D)	3.563	2.804	6.088	4.187
$\langle\alpha\rangle$ (au)	232.376	240.241	255.520	230.103

amino group are the most blue-colored regions within the MEP maps.

3.8. Global reactivity descriptors analysis

The effect of positioning the functional group in either the aromatic amine or the coupler moiety on reactivity is computed and presented in Table 2. These parameters include the absolute electronegativity (χ), hardness (η), softness (σ), chemical potential (μ), dipole moment (μ_o), and polarizability $\langle\alpha\rangle$, which were calculated according to the reported equations.[75] Notably, the positions of substituents strongly influence the quantum chemical descriptors. For instance, the computed dipole moment is an essential electronic descriptor closely related to electronic charges. The dipole moment values for dyes **D1**, **D2**, **D3**, and **D4** are 3.563, 2.804, 6.088, and 4.187 debye, respectively. As a result, the order of polarity is **D3** > **D4** > **D1** > **D2**. Relatively, the most polar compounds are those where the charge orientations are opposite, such as in the case of **D3**, and the dye **D4** in which two functional groups within the coupler structure are positioned closest to each other. In contrast, the dye with the lowest dipole moment is **D2**, where the substituents are far away from each other, resulting in a decreased dipole moment. Through all studied dyes, the dipole moment vector is oriented towards the amino phenol moiety, indicating the impact of the substituent at the amino phenol scaffold on the polarity of the molecules.

Further, the computed chemical potential for dyes **D1–D4** is negative, indicating the stability of the investigated systems. Overall, these results showcase the effectiveness of computational chemistry methods in describing molecular and electronic interactions.

3.9. RDG analysis

The RDG function is one of the most successful functions to unravel different Interactions within the molecule. The distinctive aspect of the RDG function is its ability to be graphically translated over a molecule, displaying various attractions or repulsions using particular color codes. Hydrogen bonding, a kind of attractive force, is shown by the blue color. Meanwhile, the steric repulsion is represented by red, whereas green denotes van der Waals interactions.[76]

Fig. S17† displays the RDG plots for the **D2** and **D4** compounds. An in-depth analysis of the RDG plot for the **D2** compound would provide essential insights into the impact of intermolecular forces on experimental spectra. The RDG plot shows an intense blue color between the hydroxyl group's hydrogen atom and the azo group. This could be closely linked to the experimental ^{1}H-NMR spectrum of **D2**, where the origin of the most deshielded proton at 14.10 ppm is attributed to intramolecular hydrogen bonding. This conclusion aligns with the experimental finding and could be treated as evidence for the significant impact of this intramolecular hydrogen bond interaction on the chemical shift.

The comparison of RDG for **D4** and **D2** reveals that hydrogen bonding is absent in **D2**. Consequently, the hydroxyl proton in dye **D4** is observed within the expected range for the aromatic hydroxyl group at 9.72 ppm. Additionally, both compounds exhibited steric repulsion within the aromatic moiety as a result of π electron density. Thus, it has been demonstrated that integrating RDG analysis with computed NMR spectra is essential for comprehensively interpreting the experimental NMR spectra.

3.10. Assessment of microbiological activity of the different azo dyes and structure–activity relationships

The antibacterial activity of the synthesized dyes **D1–D4** was assessed by determining the MIC against *S. aureus* (ATCC 6538) and another multi-drug-resistant MRSA clinical isolate. As shown in Table 3, **D4** showed the lowest MIC value when tested against the *S. aureus* ATCC 6538.

Investigation of the relationship between the structural characteristics of **D1–D4** and their antibacterial activities revealed that the substitution pattern of the phenolic hydroxyl group is critical. As observed, 3-((4-amino-3-hydroxyphenyl) diazenyl)benzoic acid (**D4**) showed superior antibacterial activity relative to the 2-hydroxy analogs **D1–D3**. Nevertheless, the proximity of the carboxylic acid group to the diazo group contributed to the antibacterial potency. In this regard, the 2-benzoic acid derivative **D1** showed the lowest activity among the series, whereas shifting the carboxylic group one carbon (**D2** and **D4**) or two carbons (**D3**) away from the diazo group in **D1** conferred higher activities to the scaffold. In summary, the optimum activity was observed when conserving the phenolic and carboxylic groups at position 3 *i.e.* 2 carbons away from the diazo group in the **D4** derivative.

Being the most active dye, the antibacterial activity of **D4** was further investigated. It showed good antibacterial activity against multidrug-resistant MRSA isolate at the same MIC seen with the standard strain (MIC = 78 μg mL^{-1}). That is similar to other studies that used chemically relevant dyes that showed antibacterial activity with comparable MIC towards *Staphylococcus aureus*.[77] All dyes were found to be bacteriostatic as evidenced from

Table 3 MIC and MBC values of the synthetic dyes (D1–D4) against *S. aureus* standard strain and MRSA clinical isolate

	Staphylococcus aureus ATCC 6538				MRSA clinical isolate
Dye	**D1**	**D2**	**D3**	**D4**	**D4**
MIC (μg mL^{-1})	625	312.5	312.5	78.125	78.125
MBC (μg mL^{-1})	>1250	>1250	>1250	625	625

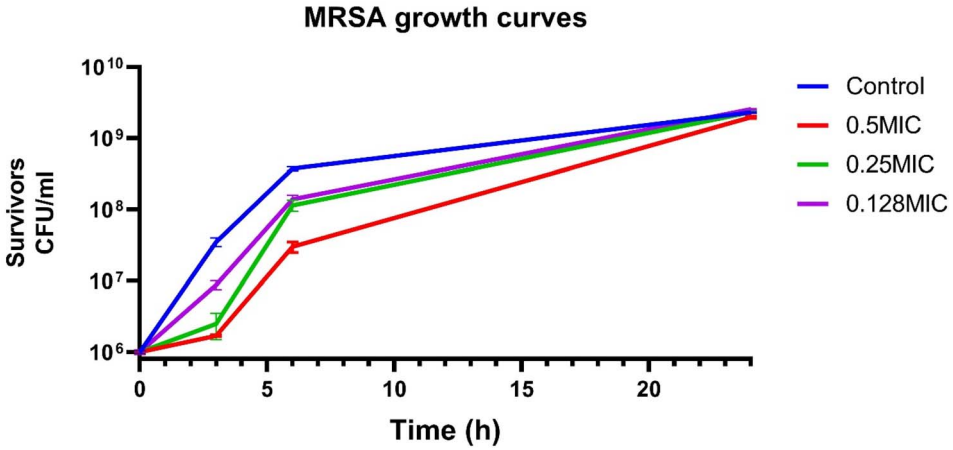

Fig. 7 Growth curves of the MRSA clinical isolate in the absence or presence of different concentrations of **D4**. Bacterial inocula were adjusted and allowed to grow without or with varying concentrations of **D4** equivalent to 0.5, 0.25, and 0.125 MIC. At different time intervals, the bacterial count was determined.

MBC values against *S. aureus* ATCC 6538 and the clinical MRSA isolate (Table 3). To assess the effect of **D4** on different stages of bacterial growth, the tested MRSA clinical isolate was grown in the presence or absence of different sub-inhibitory concentrations of **D4**. The number of survivors was determined at various time points, and bacterial growth curves were constructed for each tested concentration. **D4** at 0.25 and 0.5× MIC hindered the isolate's growth to approximately one log, relative to the untreated control, at 3 hours. This effect was maintained in the case of 0.5× MIC at 6 hours; however, regrowth occurred at the 24 hour time point (Fig. 7).

3.11. Biofilm inhibition capability of D4

A biofilm inhibition assay was done to study the ability of **D4**, the most active dye in terms of MIC, to prevent biofilm formation. Biofilm formation is a virulence factor contributing to *S. aureus* pathogenicity, leading to severe and chronic diseases.[78] Biofilm formation allows the bacterium to attach and adhere to different host tissues as well as on different implanted devices or catheter tubing. This process increases *S. aureus* virulence and resistance to antimicrobial treatment.[79,80] We tested the ability of **D4** to inhibit biofilm formation of the MRSA clinical isolate by incubating the bacterium with different concentrations of **D4** while allowing MRSA to adhere on a plastic 96 well plate. As shown in Fig. 8, **D4** was able to inhibit biofilm formation of the tested MRSA clinical isolate, which is a strong biofilm former: at a concentration of 39 μg mL^{-1} (equivalent to 0.5× MIC), **D4** was able to inhibit primarily any biofilm formation (inhibition of 97% of biofilm formation). Interestingly, even at a lower concentration equivalent to 0.25 MIC (19.5 μg mL^{-1}), around 89% of biofilm formation was inhibited. That demonstrates the anti-virulence

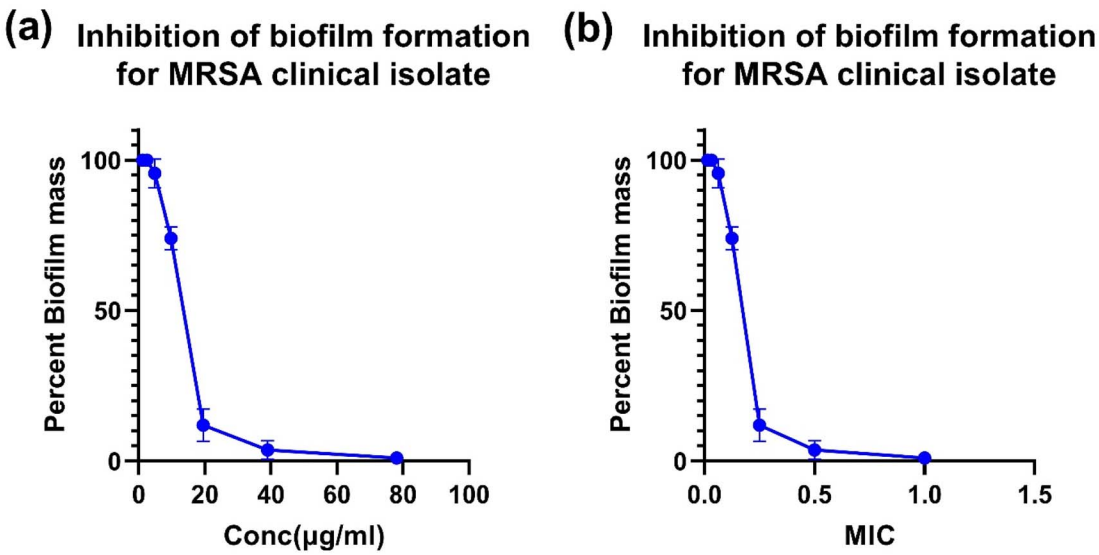

Fig. 8 Biofilm inhibition assay of dye **D4** against the strong biofilm former MRSA isolates. Bacterial inocula were allowed to form biofilm in the absence or the presence of different concentrations of **D4**. After incubation, biofilm was quantified, and the percent biofilm formation was plotted against concentrations of **D4** expressed as μg mL^{-1} in (a) or as MIC equivalent in (b).

activity of **D4** above-demonstrated. More importantly, the anti-virulence activity of **D4** can be used at sub-MIC concentrations, which may limit the development of resistance. Amengor *et al.* described a 57% inhibition of biofilm formation by *S. aureus* at 125 μg mL^{-1}.[81] Mini *et al.* reported the antibiofilm potential of carmoisine azo dye against *Pseudomonas aeruginosa*, presumably due to inhibition of quorum sensing.[82]

3.12. D4 inhibits the SaeR/S two-component regulatory system in MRSA

qRT-PCR was used to evaluate the effect of **D4** on the expression and regulation of the MRSA clinical isolate's SaeR, SaeS two-component system. SaeR/S is a regulatory system that consists of: SaeS, which is a sensor histidine kinase and SaeR, which is a response regulator. The biological importance of this two-component system is that it controls the expression of several essential virulence factors of *S. aureus*, such as alpha-hemolysin (Hla), leukocidins, and other virulence factors which are crucial for the bacterium's pathogenicity and ability to evade the immune response. Moreover, by modulating the expression of these virulence factors, the SaeR/S system helps *S. aureus* survival and its ability to promote infection by allowing the bacteria to adapt to different environmental conditions outside and within the host.[83,84] Besides, the Sae system has been known to affect biofilm formation positively or negatively depending on the strain and the environment.[85] Inhibiting the SaeR/S can be a plausible way to reduce *S. aureus* virulence. It is one of the new potential targets for novel therapeutics alone or in combination with known antibacterial agents. To provide mechanistic insights into the mechanism of **D4** antibacterial and **D4** antibacterial and anti-virulence activities, MRSA bacterial cultures were allowed to grow in the absence or presence of **D4** at its 0.5× MIC value for 24 hours. **D4** significantly reduced SaeR expression by about 2 fold as compared to the untreated control (Fig. 9). Interestingly, **D4** also significantly decreased the expression of SaeS by about 30 fold (0.03 fold change compared to normalized untreated control) (Fig. 9). These qPCR data suggest that inhibiting the SaeS/SaeR system is another potential mechanism by which **D4** exerts its antibacterial and anti-virulence effects. In a previous study, phenazopyridine hydrochloride inhibited SaeS kinase activity, ultimately decreasing the expression of toxic shock syndrome toxin (TSST-1) and reducing the virulence of *S. aureus*.[86]

3.13. Stability of dye D4 in biological medium

The stability of dye **D4** in PBS has been assessed through UV-vis measurements, which is an established technique for evaluating organic compound stability in biological media.[87] The UV-vis spectra for the MIC of the dye before and after incubation in PBS solution at 37 °C for 24 hours were illustrated in Fig. S18 (ESI).† The UV-vis spectra showed no significant changes in absorption band position, indicating that dye **D4** remained chemically stable and retained its structural integrity under these conditions. Therefore, the most potent dye is confirmed to be stable in biological medium.

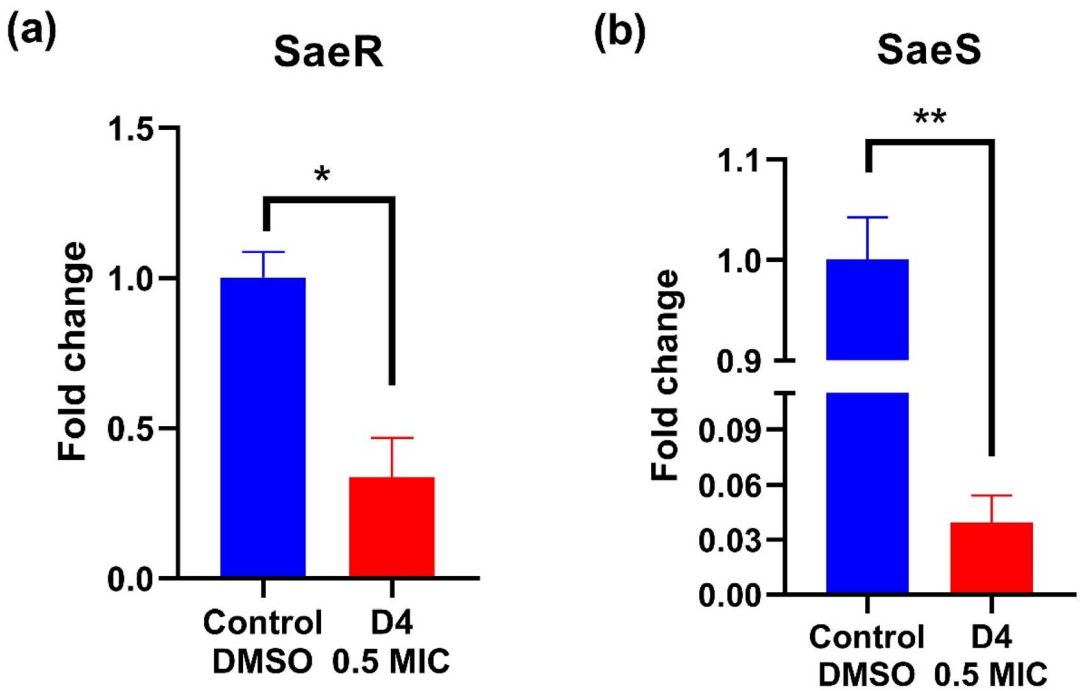

Fig. 9 **D4** significantly reduces SaeS and SaeR two-component regulatory system expression. MRSA clinical isolate was allowed to grow in the presence or absence of 0.5 MIC of **D4**. After 24 hours, RNA was extracted, and SaeS and SaeR mRNA were quantified using qPCR relative to the gyrB housekeeping gene. Fold changes were normalized relative to solvent-treated control. Student's *t*-test was used to analyze fold changes. (*, $p < 0.05$; **, $p < 0.01$).

4 Conclusion

The present study set out to design novel synthetic azo dyes derived from isomeric amino benzoic acid as potent antibacterial agents, advancing the clinical research field. This is further integrated with diverse experimental spectroscopic techniques such as UV-vis, FTIR, NMR spectroscopy, and HRMS integrated with comprehensive DFT calculations. A summary of the essential outcomes is as follows:

• Generally, the dyes were synthesized with an excellent yield, with the minimal use of hazardous organic solvents to comply with the sustainable development goals (SDGs).

• The experimental UV-vis spectra have been assigned to the corresponding transitions, elucidating the crucial influence of substituents on the photochromic properties of the dyes.

• The experimental NMR spectrum agrees with the computed one, confirming the appropriateness of the method and basis sets used for these calculations.

• Further interpretation for experimental NMR was performed by computing RDG functions. In sum, the RDG confirms strong intramolecular hydrogen bond through O–H···N interaction for dyes derived from *m*-amino phenol.

• A key strength of the present study was the proof of the exchangeability of aromatic proton within certain dyes through the utilization of HMQC to elucidate one bond coupling.

• Accurate DFT computations were conducted to find the optimal geometry of the dyes. Subsequently, global reactivity descriptors were calculated and discussed.

• The tendency of different moieties for charge donation or acceptance was designated through visualized FMOs. Meanwhile, the reactivity of atomic sites for electrophilic and nucleophilic attacks was assigned based on MEP map analyses.

• The dyes showed antibacterial activity towards the *Staphylococcus aureus* standard strain and, more importantly, against clinically isolated multidrug-resistant MRSA strain.

• One promising synthesized dye (**D4**) showed good antibiofilm activity against the tested MRSA strong biofilm former MRSA strain with about 89% biofilm inhibition with concentrations down to 0.25 MIC.

• **D4** demonstrated potential anti-virulence activity by strongly inhibiting the SaeS/SaeR two-component system, a key regulator of various bacterial-associated virulence factors.

• **D4** is a promising antibacterial dye with both antibacterial and anti-virulence properties. Its anti-virulence activity, observed at concentrations lower than its MIC, could significantly help in decreasing its resistance in bacterial systems. This makes **D4** a valuable candidate for use in clinical settings to combat multi-drug-resistant MRSA.

• Future studies should explore the potential of these dyes to be used as indicators, given their acid/base sensitivity.

Data availability

The data supporting this article have been included as part of the ESI.†

Author contributions

Ahmed M. Hegazy: conceptualization, investigation, data curation, formal analysis, visualization, writing – original draft. Michael G. Shehat: investigation, data curation, methodology, formal analysis, writing – review & editing. Alaa Abouelfetouh: funding acquisition, validation, resources, writing – review & editing. Mohamed Teleb: writing – review & editing. Sherine N. Khattab: project administration, conceptualization, methodology, resources, writing – review & editing. Nesreen S. Haiba: formal analysis, validation, writing – review & editing.

Conflicts of interest

The authors declare that they have no known competing financial interests or personal relationships that could have appeared to influence the work reported in this paper.

Acknowledgements

This study was partly supported by the German Research Council (DFG) through grant ZI665/3-2 to Dr Alaa Abouelfetouh. Additionally, the work received financial support from ICGEB and COMSTECH (Committee on Scientific and Technological Cooperation of the Organization of Islamic Cooperation), project no. CRP/EGY23-01. We express our sincere appreciation to the Royal Society of Chemistry (RSC) who provided chemist Ahmed M. Hegazy with an invaluable Researcher Development and Travel Grant (ID: D23-8142936090).

References

1 S. De Backer, J. Sabirova, I. De Pauw, H. De Greve, J.-P. Hernalsteens, H. Goossens and S. Malhotra-Kumar, *Microorganisms*, 2018, **6**, 113.
2 A. Kaushik, H. Kest, M. Sood, B. W. Steussy, C. Thieman and S. Gupta, *Pathogens*, 2024, **13**, 76.
3 M. Alseqely, M. Newton-Foot, A. Khalil, M. El-Nakeeb, A. Whitelaw and A. Abouelfetouh, *Sci. Rep.*, 2021, **11**, 4253.
4 B. A. Alghamdi, I. Al-Johani, J. M. Al-Shamrani, H. M. Alshamrani, B. G. Al-Otaibi, K. Almazmomi and N. Y. Yusof, *Saudi J. Biol. Sci.*, 2023, **30**, 103604.
5 A. R. Guerroudj, E. U. Mughal, N. Naeem, A. Sadiq, J. H. Al-Fahemi, B. H. Asghar, N. Boukabcha, A. Chouaih and S. A. Ahmed, *Spectrochim. Acta, Part A*, 2024, 124093.
6 R. I. Alsantali, Q. A. Raja, A. Y. Alzahrani, A. Sadiq, N. Naeem, E. U. Mughal, M. M. Al-Rooqi, N. El Guesmi, Z. Moussa and S. A. Ahmed, *Dyes Pigm.*, 2022, **199**, 110050.
7 R. Allen, in *Colour Chemistry*, Springer, 1971, pp. 21–36.
8 R. Khanum, R. S. Ali, H. Rangaswamy, S. S. Kumar, A. Prashantha and A. Jagadisha, *Results Chem.*, 2023, **5**, 100890.
9 A. Bafana, S. S. Devi and T. Chakrabarti, *Environ. Rev.*, 2011, **19**, 350–371.
10 R. Christie, in *Colour Chemistry*, 2001, pp. 1–11.
11 D. Dantas, A. I. Ribeiro, F. Carvalho, E. Gil-Martins, R. Silva, F. Remião, A. Zille, F. Cerqueira, E. Pinto and A. M. Dias, *Chem. Commun.*, 2023, **59**, 2791–2794.

12 H. Tavallali, A. Parhami, S. R. Dastghaib and M. A. Karimi, *Spectrochim. Acta, Part A*, 2023, **289**, 122194.
13 Y. Li, C. Cao, F. Feng, K. Fang, M. Wang, R. Xie, Z. Zhao and W. Chen, *J. Mol. Liq.*, 2023, **369**, 120864.
14 D. m. Aziz, S. A. Hassan, D. M. Mamand and K. Qurbani, *J. Mol. Struct.*, 2023, **1284**, 135451.
15 K. Mezgebe, Y. Melaku, V. P. Ramachandran and E. Mulugeta, *New J. Chem.*, 2024, **48**, 4400–4416.
16 J. D. Tadić, J. M. Lađarević, Ž. J. Vitnik, V. D. Vitnik, T. P. Stanojković, I. Z. Matić and D. Ž. Mijin, *Dyes Pigm.*, 2021, **187**, 109123.
17 K. A. Elhasany, S. N. Khattab, A. A. Bekhit, D. M. Ragab, M. A. Abdulkader, A. Zaky, M. W. Helmy, H. M. Ashour, M. Teleb and N. S. Haiba, *Eur. J. Pharm. Biopharm.*, 2020, **155**, 162–176.
18 M. N. Khan, D. K. Parmar and D. Das, *Mini Rev. Med. Chem.*, 2021, **21**, 1071–1084.
19 N. Gomez-Sequeda, M. Jimenez-Del-Rio and C. Velez-Pardo, *ACS Chem. Neurosci.*, 2024, **15**, 3563–3575.
20 G. Papayan and A. Akopov, *Photodiagnosis Photodyn. Ther.*, 2018, **24**, 292–299.
21 P. C. A. Swamy, G. Sivaraman, R. N. Priyanka, S. O. Raja, K. Ponnuvel, J. Shanmugpriya and A. Gulyani, *Coord. Chem. Rev.*, 2020, **411**, 213233.
22 K. Mezgebe and E. Mulugeta, *RSC Adv.*, 2022, **12**, 25932–25946.
23 G. Domagk, *Rev. Infect. Dis.*, 1986, **8**, 163–166.
24 S. A. Misal and K. R. Gawai, *Bioresour. Bioprocess.*, 2018, **5**, 1–9.
25 M. Pervaiz, S. Sadiq, A. Sadiq, U. Younas, A. Ashraf, Z. Saeed, M. Zuber and A. Adnan, *Coord. Chem. Rev.*, 2021, **447**, 214128.
26 M. Hauser, *J. Org. Chem.*, 1964, **29**, 3449–3450.
27 J. Chen, X. Xie, J. Liu, Z. Yu and W. Su, *React. Chem. Eng.*, 2022, **7**, 1247–1275.
28 J. Qiu, B. Tang, B. Ju, S. Zhang and X. Jin, *Dyes Pigm.*, 2020, **173**, 107920.
29 M. Toupin and D. Bélanger, *J. Phys. Chem. C*, 2007, **111**, 5394–5401.
30 L. Duarte, R. Fausto and I. Reva, *Phys. Chem. Chem. Phys.*, 2014, **16**, 16919–16930.
31 A. Demirçalı, *J. Mol. Struct.*, 2021, **1231**, 129960.
32 S. H. Alarcón, A. C. Olivieri, D. Sanz, R. M. Claramunt and J. Elguero, *J. Mol. Struct.*, 2004, **705**, 1–9.
33 V. Deneva, A. Lyčka, S. Hristova, A. Crochet, K. M. Fromm and L. Antonov, *Dyes Pigm.*, 2019, **165**, 157–163.
34 Y. Cao, J. Romero, J. P. Olson, M. Degroote, P. D. Johnson, M. Kieferová, I. D. Kivlichan, T. Menke, B. Peropadre and N. P. Sawaya, *Chem. Rev.*, 2019, **119**, 10856–10915.
35 A. M. Hegazy, N. S. Haiba, M. K. Awad, M. Teleb and F. M. Atlam, *New J. Chem.*, 2023, **47**, 16470–16483.
36 N. S. Mohamed, S. M. Ibrahim, M. M. Ahmed and A. F. Al-Hossainy, *Ind. Eng. Chem. Res.*, 2023, **62**, 4312–4327.
37 A. Z. Omar, M. A. El-Rahman, E. A. Hamed, S. K. El-Sadany and M. A. El-Atawy, *Sci. Rep.*, 2023, **13**, 7826.
38 A. M. Hegazy, N. S. Haiba, M. K. Awad and F. M. Mahgoub, *Phys. Chem. Chem. Phys.*, 2023, **25**, 9532–9547.
39 M. Bursch, J. M. Mewes, A. Hansen and S. Grimme, *Angew. Chem., Int. Ed.*, 2022, **61**, e202205735.
40 M. A. Salem, M. K. Awad, R. K. Sleet and M. A. El-Ghobashy, *Mater. Chem. Phys.*, 2024, 129795.
41 A. M. Bayoumy, A. Hessein, M. A. Belal, M. Ezzat, M. A. Ibrahim, A. Osman and A. A. El-Moneim, *J. Power Sources*, 2024, **617**, 235145.
42 F. E. H. David and L. Blangey, *Fundamental processes of dye chemistry*, Interscience publisher's ltd., London, 1949, p. 1.
43 M. Frisch and F. Clemente, G. Scalmani, V. Barone, B. Mennucci, G. A. Petersson, H. Nakatsuji, M. Caricato, X. Li, H. P. Hratchian, A. F. Izmaylov, J. Bloino and G. Zhe, *Gaussian*, vol. 9.
44 A. D. Becke, *Phys. Rev. A:At., Mol., Opt. Phys.*, 1988, **38**, 3098.
45 C. Lee, W. Yang and R. G. Parr, *Phys. Rev. B: Condens. Matter Mater. Phys.*, 1988, **37**, 785.
46 B. Mennucci, *Wiley Interdiscip. Rev.: Comput. Mol. Sci.*, 2012, **2**, 386–404.
47 K. Wolinski, J. F. Hinton and P. Pulay, *J. Am. Chem. Soc.*, 1990, **112**, 8251–8260.
48 K. Momma and F. Izumi, *J. Appl. Crystallogr.*, 2011, **44**, 1272–1276.
49 A. Frisch, A. Nielson and A. Holder, *GaussView 5.0*, Gaussian Inc., Pittsburgh, PA, 2000, vol. 556.
50 G. Andrienko, *Chemcraft, v. 1.8 (build 445)-graphical software for visualization of quantum chemistry computations*, in.
51 T. Lu and F. Chen, *J. Comput. Chem.*, 2012, **33**, 580–592.
52 W. Humphrey, A. Dalke and K. Schulten, *J. Mol. Graph.*, 1996, **14**, 33–38.
53 R. M. Humphries, J. Ambler, S. L. Mitchell, M. Castanheira, T. Dingle, J. A. Hindler, L. Koeth and K. Sei, *J. Clin. Microbiol.*, 2018, **56**, e01934.
54 L. Boge, H. Bysell, L. Ringstad, D. Wennman, A. Umerska, V. Cassisa, J. Eriksson, M.-L. Joly-Guillou, K. Edwards and M. Andersson, *Langmuir*, 2016, **32**, 4217–4228.
55 C. Rodríguez-Melcón, C. Alonso-Calleja, C. García-Fernández, J. Carballo and R. Capita, *Biology*, 2021, **11**, 46.
56 H. Lade, J. H. Park, S. H. Chung, I. H. Kim, J.-M. Kim, H.-S. Joo and J.-S. Kim, *J. Clin. Med.*, 2019, **8**, 1853.
57 M. Gomes-Fernandes, M. Laabei, N. Pagan, J. Hidalgo, S. Molinos, R. Villar Hernandez, D. Domínguez-Villanueva, A. T. A. Jenkins, A. Lacoma and C. Prat, *PLoS One*, 2017, **12**, e0175552.
58 J. Duan, M. Li, Z. Hao, X. Shen, L. Liu, Y. Jin, S. Wang, Y. Guo, L. Yang and L. Wang, *Emerg. Microb. Infect.*, 2018, **7**, 1–10.
59 J. Garcia-Amoros, A. Sanchez-Ferrer, W. A. Massad, S. Nonell and D. Velasco, *Phys. Chem. Chem. Phys.*, 2010, **12**, 13238–13242.
60 A. Georgiev, A. Kostadinov, D. Ivanov, D. Dimov, S. Stoyanov, L. Nedelchev, D. Nazarova and D. Yancheva, *Spectrochim. Acta, Part A*, 2018, **192**, 263–274.
61 A. Z. Omar, A. S. Mohamed, E. A. Hamed, S. M. El-Badry and M. A. El-atawy, *J. Mol. Liq.*, 2024, 125216.
62 Z. Lei and L. Xiaogang, *ACS Sustainable Chem. Eng.*, 2013, **1**(11), 1440–1452.
63 A. Z. Omar, A. M. Khamis, E. A. Hamed, S. K. El-Sadany, E. M. A. Rehim, M. E. Elba, M. G. Mohamed and M. A. El-Atawy, *Sci. Rep.*, 2023, **13**, 21554.

64 P. Debnath, A. Das, K. S. Singh, T. Yama, S. S. Singh, R. J. Butcher, L. Sieroń and W. Maniukiewicz, *Inorg. Chim. Acta*, 2019, **498**, 119172.
65 A. C. Olivieri, R. B. Wilson, I. C. Paul and D. Y. Curtin, *J. Am. Chem. Soc.*, 1989, **111**, 5525–5532.
66 L. Racané, Z. Mihalić, H. Cerić, J. Popović and V. Tralić-Kulenović, *Dyes Pigm.*, 2013, **96**, 672–678.
67 M. Ueda, N. Kishida, L. Catti and M. Yoshizawa, *Chem. Sci.*, 2022, **13**, 8642–8648.
68 P. S. de Carvalho, F. M. Nachtigall, M. N. Eberlin and L. A. B. Moraes, *J. Org. Chem.*, 2007, **72**, 5986–5993.
69 P. Ruggiero, F. Interesse and O. Sciacovelli, *Geochem. Cosmochim. Acta*, 1979, **43**, 1771–1775.
70 P. Ruggiero, F. Interesse, L. Cassidei and O. Sciacovelli, *Geochim. Cosmochim. Acta*, 1980, **44**, 603–609.
71 P. Ruggiero, F. Interesse and O. Sciacovelli, *Soil Biol. Biochem.*, 1981, **12**(3), 297–299.
72 K. Fukui, *Science*, 1982, **218**, 747–754.
73 Y. Huang, C. Rong, R. Zhang and S. Liu, *J. Mol. Model.*, 2017, **23**, 1–12.
74 H. Weinstein, R. Osman, J. P. Green and S. Topiol, *Chemical Applications of Atomic and Molecular Electrostatic Potentials: Reactivity, Structure, Scattering, and Energetics of Organic, Inorganic, and Biological Systems*, 1981, pp. 309–334.
75 I. Obot, D. Macdonald and Z. Gasem, *Corros. Sci.*, 2015, **99**, 1–30.
76 E. R. Johnson, S. Keinan, P. Mori-Sánchez, J. Contreras-García, A. J. Cohen and W. Yang, *J. Am. Chem. Soc.*, 2010, **132**, 6498–6506.
77 M. Pérez-Aranda, E. Pajuelo, S. Navarro-Torre, P. Pérez-Palacios, B. Begines, I. D. Rodríguez-Llorente, Y. Torres and A. Alcudia, *Antibiotics*, 2022, **11**, 1800.
78 J. L. Lister and A. R. Horswill, *Front. Cell. Infect. Microbiol.*, 2014, **4**, 178.
79 S. Hogan, N. Stevens, H. Humphreys, J. O'Gara and E. O'Neill, *Curr. Pharmaceut. Des.*, 2015, **21**, 100–113.
80 L. Barrett and B. Atkins, *J. Antimicrob. Chemother.*, 2014, **69**, i25–i27.
81 C. D. K. Amengor, F. K. Kekessie, A. Brobbey, J. N. Addotey, P. Peprah, C. Amaning-Danquah, J. Adu, M. Tetteh and E. B. A. Adusei, *Journal of Scientific Research and Reports*, 2022, **28**, 77–88.
82 M. Mini, D. Jayakumar and P. Kumar, *J. Biomol. Struct. Dyn.*, 2023, 1–11.
83 R. P. Novick and D. Jiang, *Microbiology*, 2003, **149**, 2709–2717.
84 C. Goerke and C. Wolz, *Int. J. Med. Microbiol.*, 2010, **300**, 520–525.
85 Q. Liu, W.-S. Yeo and T. Bae, *Genes*, 2016, **7**, 81.
86 K. Dufresne, D. A. DiMaggio Jr, C. S. Maduta, S. R. Brinsmade and J. K. McCormick, 2024, preprint, 2024.2002.2027.582338, DOI: **10.1101/2024.02.27.582338**.
87 M. H. Kaulage, B. Maji, S. Pasadi, S. Bhattacharya and K. Muniyappa, *Eur. J. Med. Chem.*, 2017, **139**, 1016–1029.